stress. Taken together, SF reorganization associated with cell morphological changes may play an important role in EC remodeling process.

Well-known mechanotransducers in EC remodeling to mechanical stimuli are SACs, integrins and PECAM-1. SACs are known to be activated by tension. Naruse et al. [22] reported that EC remodeling under exposure to cyclic stretch is inhibited by the blockade of SACs with $GdCl_3$ treatment. In this study, $GdCl_3$ treatment did not significantly affect either morphological changes or localization of SHP-2 at intercellular junctions, indicating that mechanotransduction of SACs does not have a pivotal role in the present EC remodeling. Osawa et al. [13] showed that when mechanotransduction by PECAM-1 occurred, SHP-2 molecules bound to phosphorylated PECAM-1 and recruited to cell-cell borders. Therefore, at least, mechanotransduction by PECAM-1 might be activated by application of local stretch in this study. A recent study [14] suggested that mechanotransduction by PECAM-1 may trigger flow-induced morphological changes of ECs. It is speculated that spatial gradient of magnitude of mechanical stimuli in cells might induce localized mechanotransduction by PECAM-1, possibly leading to the directional EC remodeling. To study this mechanism, further investigations in terms of the quantitative relationship between intracellular stress transfer and SHP-2/PECAM-1 expression should be included.

Conclusions

In this study, local stretch was applied to an EC to stimulate a neighboring EC via intercellular junctions using micromanipulation technique. ECs reorientated and elongated parallel to the direction of stretch. This remodeling process varied from cell to cell, particularly depending on initial cell shape. In addition, SHP-2 was found to be recruited to the stimulated intercellular junctions. These results strongly suggest that intercellular junctions can transmit mechanical forces between cells and transduce the forces into biochemical signals.

Acknowledgement The authors thank Dr. Ikuo Takahashi for kindly providing human umbilical cords. This work was in part supported financially by Grants-in-Aid for Scientific Research from the Ministry of Education, Culture, Sports, Science and Technology (MEXT) in Japan (Nos. 15086203, 17200030, 17680036).

Appendix. Calculation of SF parameters with image processing

The protocol for image processing to determine SF parameters is shown in Fig. 8. Algorithm based on pixel intensity of fluorescence images of GFP-actin was adapted from previous reports [23, 24]. SFs were extracted from original image [Fig. 8(a)] with convolution filter application, as shown in Fig. 8(b). For giving pixels $p_{i,j}$ in 8-bit gray-scale, the pixels surrounding $p_{i,j}$ were selected as a sample matrix [equation (1)]

$$\text{Sample matrix}(S_{i,j}) = \begin{pmatrix} p_{i-2,j-2} & p_{i-2,j-1} & p_{i-2,j} & p_{i-2,j+1} & p_{i-2,j+2} \\ p_{i-1,j-2} & p_{i-1,j-1} & p_{i-1,j} & p_{i-1,j+1} & p_{i-1,j+2} \\ p_{i,j-2} & p_{i,j-1} & p_{i,j} & p_{i,j+1} & p_{i,j+2} \\ p_{i+1,j-2} & p_{i+1,j-1} & p_{i+1,j} & p_{i+1,j+1} & p_{i+1,j+2} \\ p_{i+2,j-2} & p_{i+2,j-1} & p_{i+2,j} & p_{i+2,j+1} & p_{i+2,j+2} \end{pmatrix} \quad (1)$$

Convolution using horizontal and vertical kernels [equations (2) and (3)], which define weighted sum of neighboring pixels, provided magnitude of brightness gradient of SFs in each pixel [equation (4)].

$$\text{Vertical kernel } (K_v) = \begin{pmatrix} -1 & 0 & 2 & 0 & -1 \\ -2 & 0 & 4 & 0 & -2 \\ -4 & 0 & 8 & 0 & -4 \\ -2 & 0 & 4 & 0 & -2 \\ -1 & 0 & 2 & 0 & -1 \end{pmatrix} \quad (2)$$

$$\text{Horizonal kernel } (K_h) = K_v^T \quad (3)$$

$$G = S_{i,j} * K_h + S_{i,j} * K_v \quad (4)$$

The pixel whose G value was bigger than 5-fold of averaged pixel intensity in whole area of the target cell was assigned as a constituent of SFs. In order to calculate the angle of SF orientation, the angle of minimal gradient in pixel intensity in each pixel [Fig. 8(c)] was calculated using Sobel kernels as previously reported [20]. The angle data allocated to only pixels which have been assigned as a constituent of SFs [Fig. 8(d)]. Angle values were summed up across the cell with vectorial summation and were assumed that each pixel has a vector consisted of the calculated angle and unit length. The angle between the direction of the resultant vector and the tensile direction was defined as the angle of SF orientation. The length of the resultant vector divided by the number of pixels was defined as the uniformity index of SFs, which indicate the degree of alignment of SFs. All calculation processes were executed on Excel 2004 for Mac (Microsoft, USA). Analyses were performed on images obtained at every 5 min after application of local stretch.

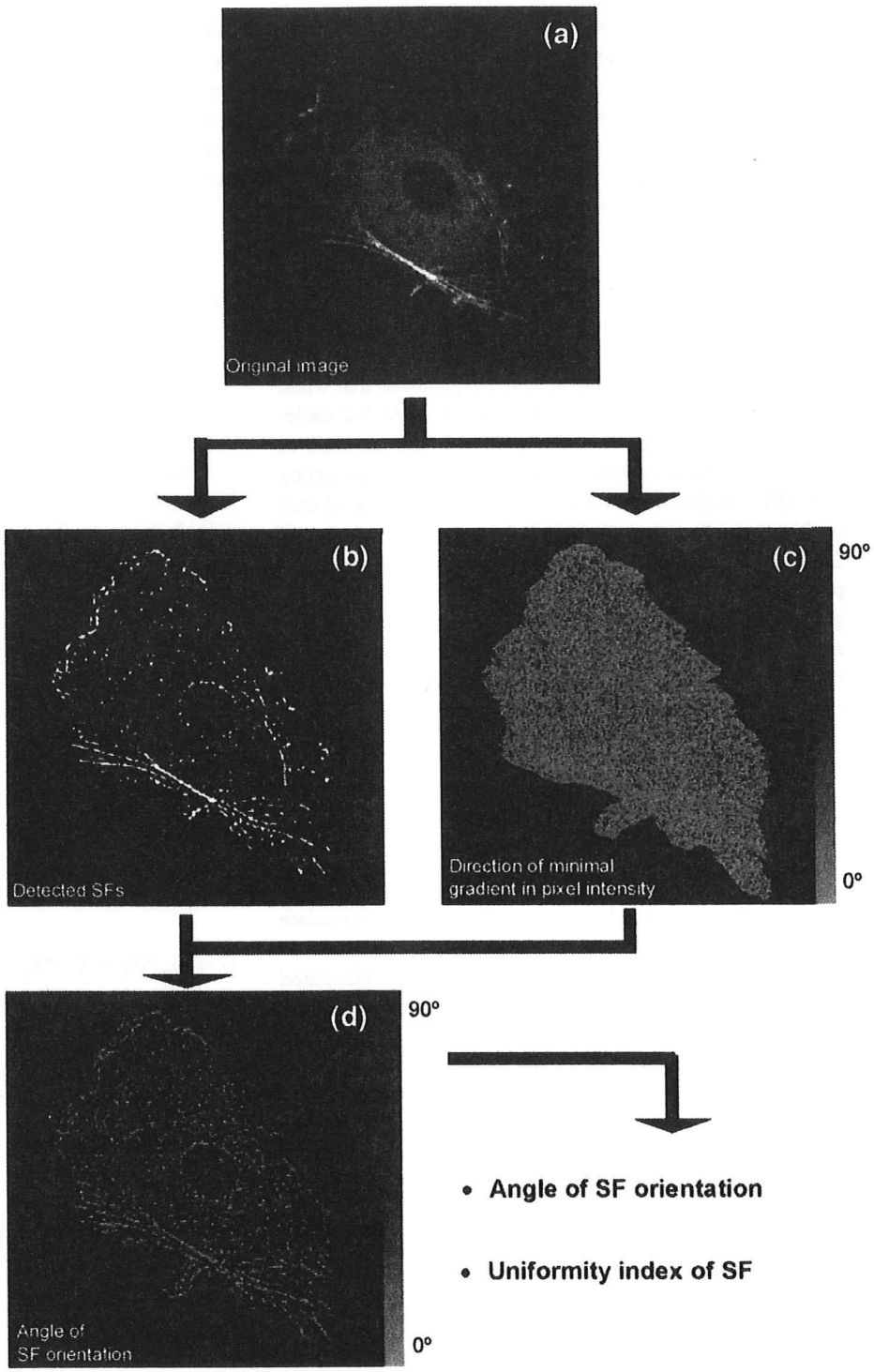

Fig. 8 Protocol for determination of SF parameters based on image processing. (**a**) Manually extracted single cell image, (**b**) automatically detected SFs with convolution filters, (**c**) calculated minimal gradient in pixel intensity with Sobel filter, (**d**) angle of SF orientation in each pixel

References

1. Dewey CF, Bussplari SR, Gimbrone MA, Davies PF (1981) The dynamic response of vascular endothelial cells to fluid shear stress. J Biomech Eng 103:177–185.
2. Galbraith CG, Skalak R, Chien S (1998) Shear stress induces spatial reorganization of the endothelial cell cytoskeleton. Cell Motil Cytoskelet 40:317–330.
3. Sato M, Nagayama K, Kataoka N, Sasaki M, Hane K (2000) Local mechanical properties measured by atomic force microscopy for cultured bovine endothelial cells exposed to shear stress. J Biomech 33:127–135.
4. Kataoka N, Ujita S, Sato M (1998) The effect of flow direction on the morphological responses of cultured bovine aortic endothelial cells. Med Biol Eng Comput 36:122–128.
5. Shirinsky VP, Antonov AS, Birukov KG, Sobolevsky AV, Romanov YA, Kabaeva NV, Antonova GN, Smirnov VN (1989) Mechano-chemical control of human endothelium orientation and size. J Cell Biol 109:331–339.
6. Wang JH, Goldschmidt-Clermont P, Wille J, Yin FC (2001) Specificity of endothelial cell reorientation in response to cyclic mechanical stretching. J Biomech 34:1563–1572.
7. Sugaya Y, Sakamoto N, Ohashi T, Sato M (2003) Elongation and random orientation of bovine endothelial cells in response to hydrostatic pressure: comparison with response to shear stress. JSME Int J Ser C 46:1248–1255.
8. Ohashi T, Sugaya Y, Sakamoto N, Sato M (2007) Hydrostatic pressure influences morphology and expression of VE-cadherin of vascular endothelial cells. J Biomech 40:2399–2405.
9. Albelda SM, Muller WA, Buck CA, Newman PJ (1991) Molecular and cellular properties of PECAM-1 (endoCAM/CD31): a novel vascular cell-cell adhesion molecule. J Cell Biol 114:1059–1068.
10. Ilan N, Cheung L, Pinter E, Madri JA (2000) Platelet-endothelial cell adhesion molecule-1 (CD31), a scaffolding molecule for selected catenin family members whose binding is mediated by different tyrosine and serine/threonine phosphorylation. J Biol Chem 275:21435–21443.
11. Kataoka N, Ujita S, Kimura K, Sato M (1998) The morphological responses of cultured bovine aortic endothelial cells to fluid-imposed shear stress sparse and colony conditions. JSME Int J Ser C 41:76–82.
12. Masuda M, Fujiwara K (1993) Morphological responses of single endothelial cells exposed to physiological levels of fluid shear stress. Front Med Biol Eng 5:79–87.
13. Osawa M, Masuda M, Kusano K, Fujiwara K (2002) Evidence for a role of platelet endothelial cell adhesion molecule-1 in endothelial cell mechanosignal transduction: is it a mechanoresponsive molecule? J Cell Biol 158:773–785.
14. Tzima E, Irani-Tehrani M, Kiosses WB, Dejana E, Schultz DA, Engelhardt B, Cao G, DeLisser H, Schwartz MA (2005) A mechanosensary complex that mediates the endothelial cell response to fluid shear stress. Nature 437:426–431.
15. Sakamoto N, Ohashi T, Sato M (2001) Effect of magnetic field on nitric oxide synthesis of cultured endothelial cells. Int J Appl Electromagn Mech 14:317–322.
16. Sokabe M, Hayakawa K, Tatsumi H (2005) Varieties of mechanotransduction: the cytoskeletal stress fibre as a force transmitter and a mechanosensor. Proc Aust Physiol Soc 36:95.
17. Sasamoto A, Nagino M, Kobayashi S, Naruse K, Nimura Y, Sokabe M (2005) Mechanotransduction by integrin is essential for IL-6 secretion from endothelial cells in response to uniaxial continuous stretch. Am J Physiol, Cell Physiol 288:C1012–1022.
18. Ohashi T, Sugawara H, Matsumoto T, Sato M (2000) Surface topography measurement and intracellular stress analysis of cultured endothelial cells exposed to fluid shear stress. JSME Int J Ser C 43:780–786.
19. Tzima E, Del Pozo MA, Kiosses WB, Mohamed SA, Li S, Chien S, Schwartz MA (2002) Activation of Rac1 by shear stress in endothelial cells mediates both cytoskeletal reorganization and effects on gene expression. EMBO J 21:6791–6800.
20. Noria S, Xu F, McCue S, Jones M, Gotlieb AI, Langille BL (2004) Assembly and reorientation of stress fibers drives morphological changes to endothelial cells exposed to shear stress. Am J Pathol 164:1211–1223.
21. Li S, Chen BP, Azuma N, Hu YL, Wu SZ, Sumpio BE, Shyy JY, Chien S (1999) Distinct roles for the small GTPases Cdc42 and Rho in endothelial responses to shear stress. J Clin Invest 103:1141–1150.
22. Naruse K, Yamada T, Sokabe M (1998) Involvement of SA channels in orienting response of cultured endothelial cells to cyclic stretch. Am J Physiol 274:H1532–1538.
23. Yoshigi M, Clark EB, Yost HJ (2003) Quantification of stretch-induced cytoskeletal remodeling in vascular endothelial cells by image processing. Cytometry A 55:109–118.
24. Kaunas R, Nguyen P, Usami S, Chien S (2005) Cooperative effects of Rho and mechanical stretch on stress fiber organization. Proc Natl Acad Sci 102:15895–15900.

Journal of Biomechanical Science and Engineering

Vol. 4, No. 3, 2009

Novel Image Analysis for Trajectory of Microtubules Gliding on Kinesins with Tip Detection*

Shukei SUGITA**, ***, Naoya SAKAMOTO****, Toshiro OHASHI****, ***** and Masaaki SATO**, ****

**Department of Biomedical Engineering, Graduate School of Biomedical Engineering, Tohoku University,
6-6-01 Aramaki-aza-Aoba, Aoba, Sendai 980-8579, Japan
*** Present address: VCAD System Research Program, RIKEN,
2-1 Hirosawa, Wako 351-0198, Japan
E-mail: ssugita@riken.jp
****Department of Bioengineering and Robotics, Graduate School of Engineering, Tohoku University,
6-6-01 Aramaki-aza-Aoba, Aoba, Sendai 980-8579, Japan
*****Present address: Division of Human Mechanical Systems and Design, Graduate School of Engineering, Hokkaido University,
N13, W8, Kita, Sapporo 060-8628, Japan

Abstract

Control of the gliding directions of kinesin-driven microtubules (MTs) *in vitro* has good feasibility for the development of nano-scale transport systems. A requirement for the control of transporters in these systems includes detecting the positions of gliding MTs; however, no studies have reported on the monitoring of the positions of gliding MTs. Here, we suggest an algorithm to detect tip coordinates of gliding MTs by binarization, skeletonization, and filtration of fluorescent images of MTs. The algorithm was first applied to artificially drawn segments with given lengths (10–80 pixels), widths (1–10 pixels), and curvature radii (20–120 pixels) to verify the effect of the sizes of MTs on accuracy of tip coordinates extracted by the algorithm, and error was estimated by referring to the true coordinates. The estimated errors were as small as 2 pixels in the width and were not affected by the length and the curvature radius, indicating that our algorithm is useful to extract the tips of MTs. The algorithm was subsequently applied to images of gliding MTs. Since distances from the trajectories of the MTs to the centers of gravity of the MTs (3.7 ± 2.1 pixels) were significantly larger than those to the tips (1.9 ± 0.5 pixels), the use of the tips as representative points of gliding MTs was verified. A detection method using tips of MTs, as suggested in this study, may be a useful technique for monitoring each MT in nanoscale transport systems.

Key words: Image Analysis, Tip Detection, Microtubule, Kinesin, Nano-Scale Transport System

1. Introduction

Kinesins are nano-scale motors that move along cytoskeletal networks of microtubules (MTs) in cells to efficiently transport vesicles and protein complexes using the energy released from ATP hydrolysis [1, 2]. The gliding movements between kinesins and MTs have recently been suggested for the development of nano-scale transport systems that can transport nano-scale objects such as DNA [3] and antibodies [4] on a chip [5]. An inverted

*Received 1 July, 2009 (No. 09-0299)
[DOI: 10.1299/jbse.4.404]

gliding assay, in which filaments glide on a protein-coated surface of a chip, has often been used for reconstruction of kinesin-MT transport systems *in vitro* [6].

Key requirements for the development of the transport systems include both controlling the gliding directions of MTs and monitoring their positions. Since MTs move in random directions on a kinesin-coated surface, a number of studies have tried to control these gliding directions of MTs with chemical patterns of motor proteins [7], fabricated topographical guides [4, 8], or a combination of these two techniques [9–11]. These methods allow most MTs to be guided in pre-determined patterns on a surface. In order to control the gliding directions of individual MTs, several groups have applied electrical fields and demonstrated the ability to steer gliding MTs in desired directions [12, 13]. While the directions of the applied electric fields were manually determined in these studies, this technique could lead to the development of flexible and efficient transport systems that control the directions of each transporter independently if the positions of the MTs could be detected automatically. However, there are no reports on monitoring the positions and motion of gliding MTs. For the development of the transport system, in which gliding MTs are independently directed with external controls, such as electric fields, the detection of the position and the movement (i.e., trajectory) of each MT is required.

The center of gravity is generally used for the representative point of a moving object. However, for the case of gliding MTs *in vitro*, the shapes of the gliding MTs must be considered. MTs sometimes exhibit curved shapes due to changes in the gliding directions, which may cause their centers of gravity to be at a greater distance from their trajectories, especially for longer MTs with smaller curvature radii. When an MT is propelled by several kinesins in the direction of their long axis, it is assumed that the trajectory of the MT is determined by the position of the kinesin that has captured the leading tip of the MT, and the remaining part of the MT follows the trajectory of the tip (Fig. 1). In these situations, the leading tip of the gliding MT should be a better marker for representing the position of the MT; however, to our knowledge, no studies have evaluated the efficiency of tracking the tips of MTs gliding on kinesins.

In the present study, we developed an algorithm that extracts tips of MTs using a kernel on binarized fluorescent images and evaluated the efficiency of using the tips as representative points of the movements of the gliding MTs. We first apply the algorithm to sample segments drawn from given coordinates, and verify the tip extraction by comparing extracted coordinates to the given coordinates. We subsequently apply the algorithm to images of gliding MTs and the coordinates of the tips of the MTs are compared to the trajectories of the MTs.

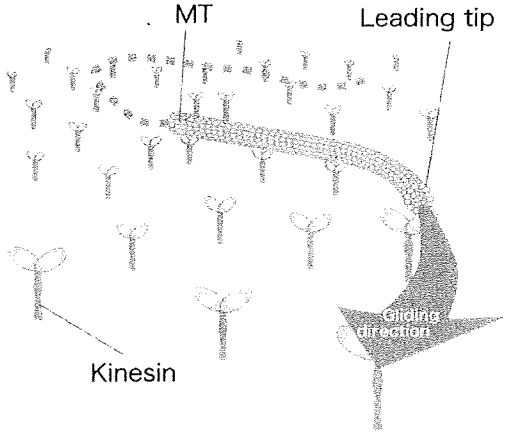

Fig. 1 A schematic of a gliding MT on a kinesin-coated surface. The gliding directions of the MT are assumed to be determined by the positions of kinesins capturing the MT.

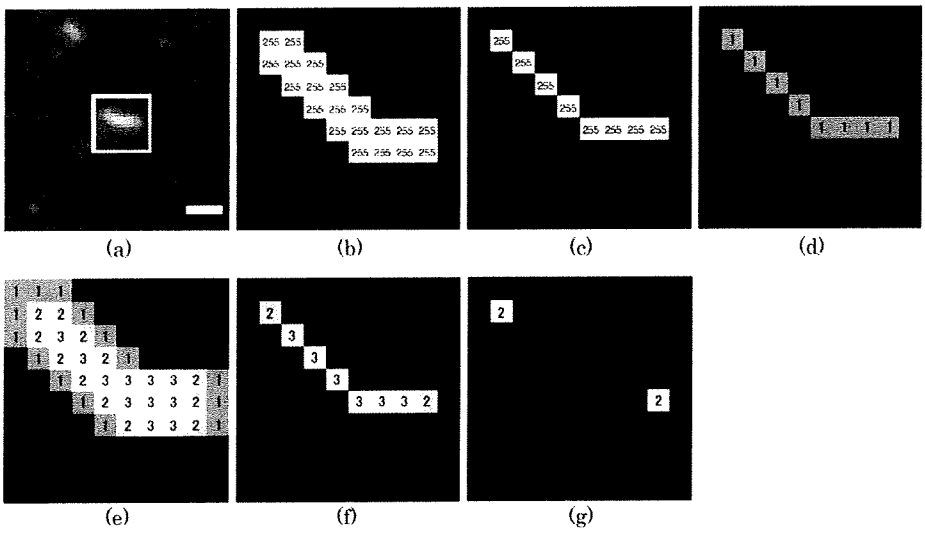

Fig. 2 Process for extracting tips of a single MT. Sample fluorescent image of the MT (a) was binarized (b), skeletonized (c), divided by 255 (d), and filtered with 3 × 3 kernel (e). Then, multiplication between the images (d) and (e) was performed (f), and finally, a binarizing process produced the extraction of the tips (g). The number in the illustrations shows the intensities in pixels; an intensity of 0 is omitted in these illustrations. Scale bar in (a) = 3 μm.

2. Analysis

2.1. Algorithm of image analysis

Analyses were conducted using an image analysis software (ImageJ, National Institutes of Health, Bethesda, MD, USA) on a personal computer (Intel Pentium 4, Microsoft Windows XP professional). Image processing was conducted by running a created macro in the software.

A schematic of the process to extract the tips of a line-shaped object in an image is shown in Fig. 2. This algorithm utilizes the property that only the end points of line-shaped objects have intensities of 2 after filtering with a kernel. An 8-bit grayscale image (Fig. 2(a)) was binarized with an appropriate threshold value by comparing with naked-eye detection of the MTs contours (Fig. 2(b)), and Zhang-Suen skeletonization [14] was performed to the image to generate an object 1 pixel wide (Fig. 2(c)). After the intensity of each pixel for the skeletonized image was divided by 255, in order to make pixels representing the line-shaped object have an intensity value of 1 and background a value of 0 (Fig. 2(d)), a filter with a 3 × 3 kernel with values of 1 for all was applied to the image (Fig. 2(e)). This process makes the resultant intensities of the end points 2. Then, multiplication was performed between the skeletonized image (Fig. 2(d)) and the filtered image (Fig. 2(e)), changing the intensities of all the pixels to 0 except the intensities those of the line-shaped object (Fig. 2(f)). Finally, the image was binarized with a threshold level of 2 to leave only the pixels whose intensities were 2. As a result, only the end points of the line-shaped object were extracted from the image (Fig. 2(g)).

2.2. Verification of image analysis

Coordinates of the tips extracted by the algorithm were compared to true coordinates of the tips of sample segments made from given coordinates to verify accuracy of the algorithm. First, we drew sample segments between given end points using the drawing tools of the image analysis software. The algorithm was applied to the image, and the tip coordinates extracted by the algorithm were compared to the given coordinates. The accuracy of the algorithm was evaluated by an error that was defined as the Euclidean distance between both the coordinates. Since MTs on fluorescent images exhibit a variety of

shapes (i.e., 3–5 pixels in width, more than 20 pixels in length, and more than 20 pixels in curvature radius (Fig. 5)) in our experimental setup (see 2.3), lengths (10, 20, 50, and 80 pixels), widths (1–10 pixels), and curvature radii (20, 40, 60, 80, 100, and 120 pixels) of sample segments were drawn to evaluate effects of object shape on estimated errors. Segments were also analyzed every 2° from 0–360°. The angle was defined by the horizontal line of the images and the line of the segment.

2.3. Image analysis of gliding microtubules

The images of gliding MTs were taken as previously reported [15]. Briefly, bovine tubulin containing 20% rhodamine-labeled tubulin were mixed and polymerized into MTs in BRB80 buffer (80 mM PIPES, 1 mM EGTA, 4 mM $MgSO_4$, pH 6.9) including 1 mM GTP at 37°C. We used the *Drosophila* kinesin with biotin carboxyl carrier protein at the C-terminal [16], which was kindly provided by Prof. H. Higuchi (University of Tokyo, Japan). To observe the gliding MTs *in vitro*, a flow cell fabricated with coverslips and spacers was sequentially filled with three kinds of protein solutions: 2 mg/ml biotinamidocaproyl labeled bovine serum albumin (biotinylated BSA), 2 mg/ml streptavidin solution, and 38 μg/ml of kinesin solution. The flow cell was then filled with 1 mM AMP-PNP solution containing MTs, followed by replacement with 1 mM ATP solution containing oxygen scavenger additives (1.5% β-mercaptoethanol, 1.5 mg/ml bovine serum albumin, 15 μM paclitaxel, 30 mM glucose, 120 μg/ml glucose oxidase, 30 μg/ml catalase) and 0.2% methylcellulose.

Time-lapsed images of the gliding MTs were captured with an inverted fluorescent microscope (IX-71, Olympus, Tokyo, Japan) equipped with a digital CCD camera (Cascade 512B, Nippon Roper, Tokyo, Japan). The rhodamine-labeled MTs were observed through a filter unit (U-MWIG, Olympus) and 60× oil immersion lens (NA = 1.45, Olympus, PLAPON 60XTIRFM). Images captured by the CCD camera were acquired using a personal computer every 1 s for 60 s, for a total of 61 slices of pixel images (512 × 512). The resolution of each image was 4 pixels/μm. The experiments were performed at room temperature of 20°C controlled by air conditioning.

Before applying the algorithm to the captured 8-bit grayscale images of MTs, the following image processing was conducted to produce well-contrasted images of smooth-shaped MTs: subtraction of background, enhancement of contrast, the application of a median filter, and binarization. This processing was first performed on the image at 0 s and the processed condition was then similarly applied to all the other images. The developed algorithm was then applied to the binarized images to extract the tips of the MTs. To evaluate the effect of changes in the threshold levels of the binarization on coordinates of the tips extracted by the algorithm, the images of smooth-shaped MTs were also binarized using higher and lower thresholds. The higher and lower thresholds were determined from levels that made the size of the MTs approximately 1 pixel bigger and 1 pixel smaller than the optimized size, respectively.

To compare the coordinates of the tips obtained in this study to general representative points of the positions of objects, coordinates of the centers of gravity of the MTs were also measured from the binarized images as stated above. Subsequently, the minimum distances from the coordinates of the tips and the centers of gravity to the trajectories of the MTs were calculated. The trajectories of the MTs were obtained from a total maximum projection image computed from time-lapsed images of the gliding MTs followed by a skeletonizing process. The mean of data for each MT was determined and is shown as mean ± standard deviation (SD). A Wilcoxon signed-ranks test was used to test for significant differences between the distances from the tips and the centers of gravity of MTs, with the level of significance at $p < 0.05$.

3. Results

3.1. Verification of algorithm

A typical image of a sample segment (5 pixels in width and 30 pixels in length), representative of the size of MTs on fluorescent images in our experiment, is shown in Fig. 3(a). By applying the algorithm to the image, the tips of the sample segment were extracted, as shown in Fig. 3(b). A merged image of the original segment and the extracted tips show that the extracted tips are located near the ends of the sample segment (Fig. 3(c)).

The effect of widths on errors for sample segments 30 pixels in length is shown in Fig. 4(a). There were no errors for sample segments 1 pixel in width, and the errors proportionally increased with an increase in width. The proportionality constant was 0.50, indicating that the errors were comparable to approximately half of the width of the sample segments. Since widths of MTs in fluorescent images ranged from 3 to 5 pixels in our experimental setup, the errors caused by the widths of the MTs on the images were estimated to be approximately 2 pixels. Effects of lengths and curvature radii of sample segments on errors are shown in Fig. 4(b) and (c), respectively. The errors did not change with any changes in the length and curvature radii of the segments. The effect of the angles of segments in images on errors is shown in Fig. 4(d). Although even small changes in angle affect the errors (approx. 2 pixels), these errors associated with changes in the angle were nearly constant. The changes in both the length and the curvature radius did not affect the errors, and although the widths of the segments did cause errors of only 2 pixels in the coordinates, we confirmed that the algorithm is applicable to extract the tip coordinates of MTs on fluorescent images.

3.2. Applying algorithm to images of gliding microtubules

Typical images of the tips of MTs, extracted using the algorithm, are shown in Fig. 5. As shown in Fig. 5(a)–(c), MTs polymerized *in vitro* have different lengths ranging from several pixels to approximately 50 pixels. Moreover, gliding MTs suddenly change their directions on the kinesin-coated surface and sometimes exhibit curved shapes. Curvature radii, calculated from arcs that passed through both end points of the MTs and had a least squares distance from points of the skeletonized MTs, were broadly distributed from 21 to more than 100 pixels (Fig. 5(d)–(f)). We assumed that the extracted coordinates of the tips of the MTs were not affected by the differences in MT length and curvature radii as indicated by the results of verifying the algorithm. In addition to the extracted tips of the MTs, the algorithm extracted midpoint of the MT shown in Fig. 5(f) because the shape of the MT after binarization exhibited a protrusion at the midpoint. In order to remove these undesirable points, the contours of the MTs should be smooth, and further improvements in image processing before application of the developed algorithms is required.

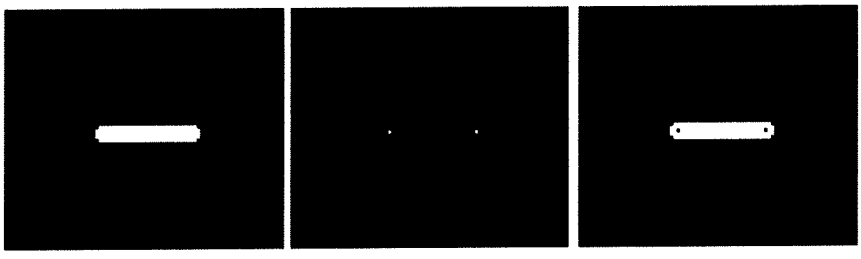

(a) (b) (c)

Fig. 3 Images of a sample segment and extracted tips. (a) A segment, 5 pixels in width and 30 pixels in length, generated from given coordinates. (b) Tips extracted by the algorithm from an image (a). (c) The sample segment merged with the tips obtained by subtracting image (a) from image (b).

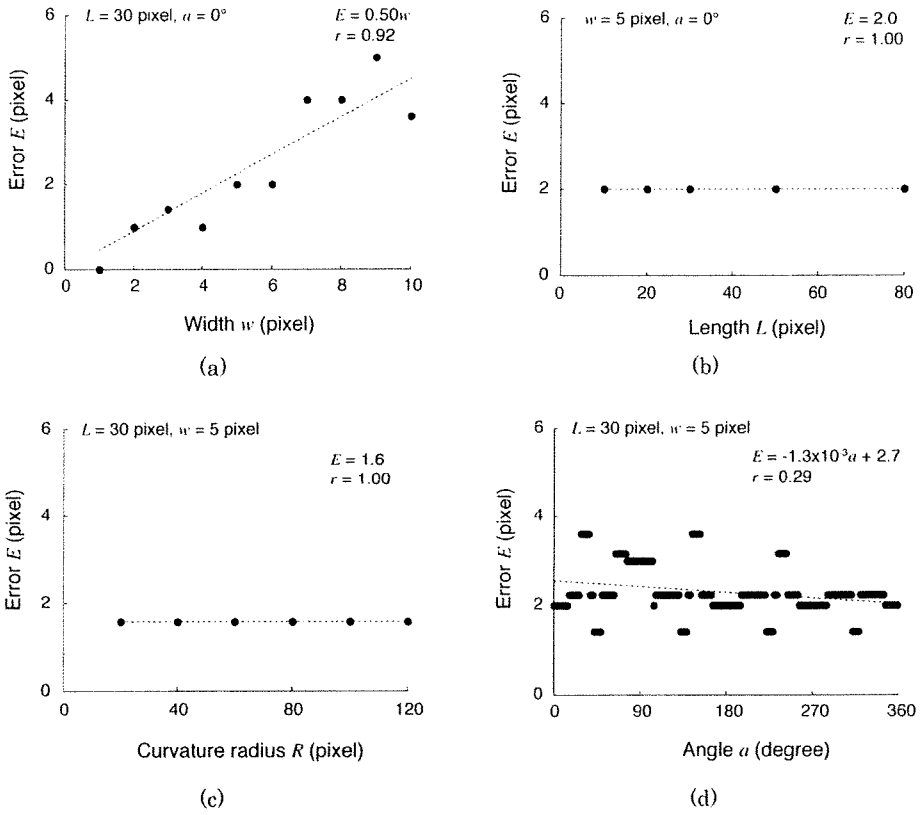

Fig. 4 Effects of (a) width, (b) length, (c) curvature radius, and (d) angle of sample segments on errors of coordinates of tips extracted by the algorithm. Dotted lines were obtained by least squares regression.

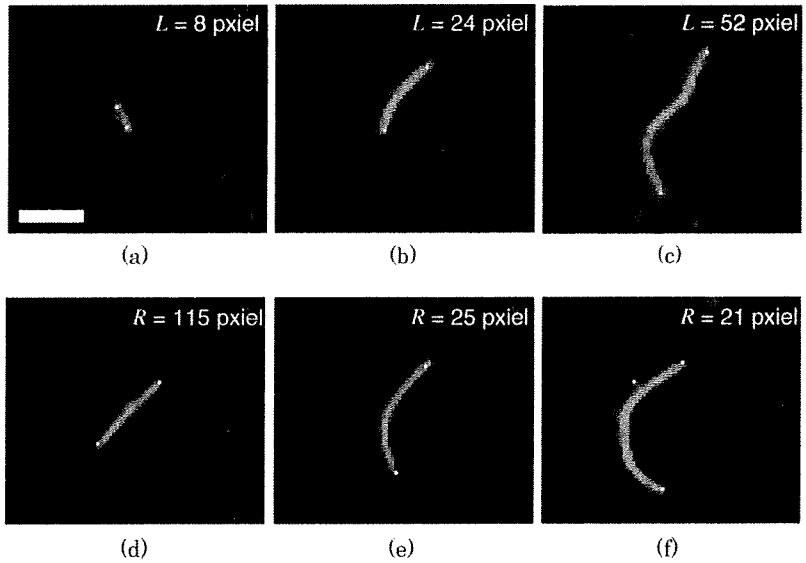

Fig. 5 Typical images of MTs (green) and extracted tips by the algorithm (white dots). Scale bar = 5μm. The MTs observed had a variety of lengths, such as L = (a) 8, (b) 24, and (c) 52 pixels, and curvature radii, such as R = (d) 115, (e) 25, and (f) 21 pixels.

Typical sequential images of the trajectory of a tip of a gliding MT is shown in Fig. 6(a). Although the trajectory of the MT obtained by superimposing the sequential images (Fig. 6(b)) was in good agreement with that of the tips extracted by the algorithm (Fig. 6(c)), a trajectory of the centers of gravity of the gliding MT merged with the Fig. 6(b) did not follow the trajectory of the gliding MT (Fig. 6(d)). The distances from the trajectories of the MTs to their tips were 1.9 ± 0.5 pixels (n = 10); significantly smaller than the distances from the trajectories of the MTs to their centers of gravity, 3.7 ± 2.1 pixels (n = 10) (Fig. 6(e)). The distances from the trajectories of the MTs to their centers of gravity were widely distributed from 1.4–7.3 pixels, whereas the distance to their tips was small (1.0–2.9 pixels). The larger distances to the centers of gravity were caused by the curved shape of the gliding MTs. In fact, there was a significant correlation between the distances to the centers of gravity and the angles, determined by dividing the lengths by the curvature radii (r = 0.746; $p < 0.001$; n = 487; data not shown). These results indicate that the distance to the centers of gravity increases for longer MTs exhibiting smaller curvature radii.

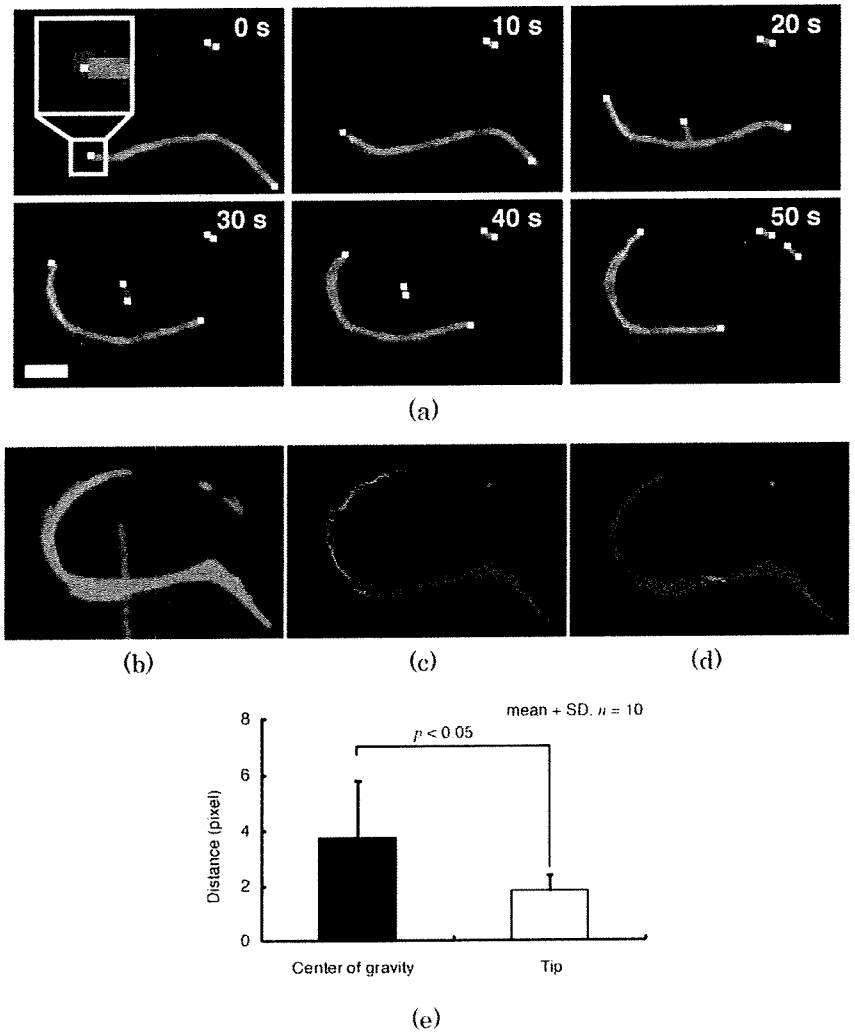

Fig. 6 Comparison between tips and centers of gravity of gliding MTs. (a) Time-lapsed images of the MTs gliding on a kinesin-coated surface merged with the images of end points (white dots) extracted by the algorithm and the trajectories of the tips (red lines). The end points extracted by the algorithm are enlarged to improve visibility, except in the inset image at 0 s. (b) Typical images of trajectories of gliding MTs. (c and d) Trajectories of (c) tips and (d) centers of gravity of the MTs (red lines) merged with (b). (e) Comparison of the minimum distances from tips and centers of gravity to trajectories of gliding MTs. Scale bar = 5 μm.

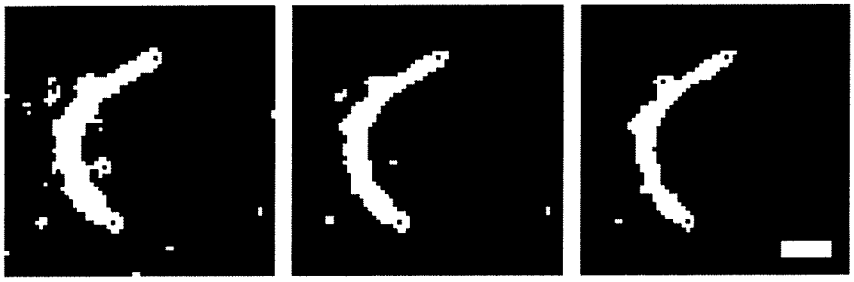

Fig. 7 Effect of threshold on changes in positions of tip coordinates (black dot in MT). The images were binarized by (a) low, (b) intermediate, (c) and high threshold levels. Scale bar = 3 μm.

The effect of thresholds for binarization on changes in the position of the tip coordinates of an MT extracted by the algorithm is shown in Fig. 7. Although the shape was bigger when the threshold level was lower, this did not affect the tip coordinates binarized with different threshold levels. The differences in tip coordinates at varying thresholds were 0.9 ± 0.9 pixels (low–intermediate, n = 155) and 1.1 ± 1.5 pixels (intermediate–high, n = 153).

4. Discussion

The center of gravity has generally been used as a representative position of an object. However, is the detection of the position of the center of gravity efficient as the representative position of the movement when a long and thinly-shaped object, such as an MT, produces a curvature radius by changing their gliding direction? The present study confirmed that the centers of gravity of MTs did not follow the trajectories of the gliding MTs, whereas their tips were in good agreement with these trajectories, as shown in Fig. 6. Therefore, the tips of MTs are important in representing the positions of gliding MTs.

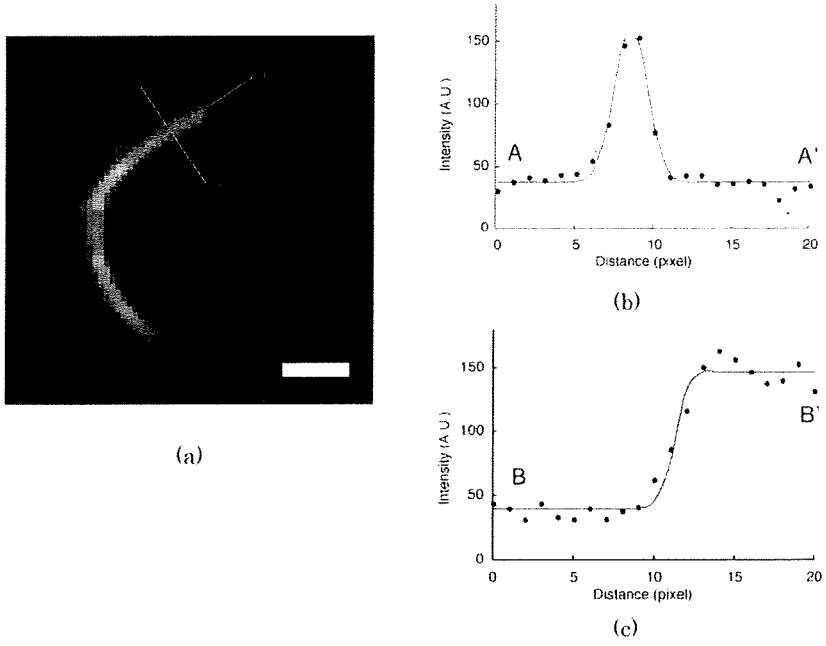

Fig. 8 Typical intensity profiles of an MT in long and short axis directions. From a fluorescent image of the MT (a), intensity profiles were measured in (b) short (A–A' in (a)) and (c) long (B–B' in (a)) axis directions. Scale bar = 3 μm. Curves fitted to (b) and (c) were determined as Gaussian and half Gaussian functions, respectively, by least squares regression.

Verification of the algorithm determined that lengths and curvature radii of sample segments did not affect errors, but increases in the width of sample segments increased the errors, and that the process of skeletonizing in the algorithm may have resulted in these errors. The skeletonizing process removes the intensities in pixels of objects from all edges until the objects have a width of 1 pixel. This process made the positions of the tips of the sample segments extracted by the algorithm located in long axis directions of the sample segments a half of the width, and was in a good agreement with the results suggesting that errors were expressed as $E = 0.50w$ in Fig. 4(a). However, the errors from the widths of the gliding MTs in fluorescent images were as small as 2 pixels in our experimental setup, and our algorithm was useful as a first step for automated extraction of the tips of MTs.

For the images of MTs, the tips of MTs extracted by the algorithm seemed to be located on the inside edges of the shapes of the MTs. Although a diameter of an MT is approximately 30 nm, the widths of the MTs observed in binarized images were measured as almost 1 μm, indicating that the width of the MTs has increased in the fluorescent images. Since the irradiation of light from a single point source causes an intensity distribution around the center of the source on an image, known as point-spread function, the spread in the width of MTs seemed to be caused by this distribution. This indicates that spreading should have occurred in long axis directions of the MTs as well; therefore, we analyzed fluorescent intensity profiles around the edges of an MT in both long and short axis directions, as shown in Fig. 8(a). For approximation of the intensity profiles, we used a Gaussian function that is often used for expressing the point-spread function [17], and results suggest that the intensity profiles can be well approximated with the Gaussian function and the half Gaussian function for the short (Fig. 8(b)) and long (Fig. 8(c)) axis directions, respectively. These results further indicate that the contours of the MTs in the fluorescent images spread in the long axis direction, and that the actual positions of tips of MTs are located inside rather than at the edge of binarized images of the MTs in the long axis direction. Although this may cause errors in estimates of the tip position, the errors would be on the order of 500 nm, thereby making the proposed algorithm effective for practical use.

Since the regulation of thresholds for binarization generally results in changes in the sizes of objects in grayscale images, we had first expected a displacement in tip coordinates of MTs when changing the threshold levels. However, differences in the tip coordinates were not observed for the three threshold levels tested (Fig. 7), and we believe that this resulted from the skeletonizing process. As shown in Fig. 8, the intensities gradually increase from the edges to the center of the MT indicating that the changes in the threshold levels cause the changes in the size of binarized MTs equivalently, in all directions. Since the size of the spreading object is decreased in all directions by the skeletonizing process, the tip coordinates extracted by the algorithm were not displaced from the changes in the threshold levels.

The skeletonizing process was conducted with the Zhang-Suen algorithm [14] which based on two subiterations. The first subiteration removes only the southeast boundary points and the northwest corner points, and the second subiteration removes northwest boundary points and the southeast corner points. Although this sequential two-step approach may generate errors 1 pixel by firstly removing the points of the one-side of objects, it is not considered to be large for practical use. In Fig. 4(d), errors caused by the changes in angles of segments were not cyclically changed with the period of 90° for some intervals of the angles (28–36°, 64–74°, 76–104°, 144–152°, 234–242°). In the angles, extracted tip coordinates was located 1 pixel horizontally or vertically distant from the periodically estimated coordinates. Therefore, differences of the errors from the periodical value are considered to be caused by the sequential two-step approach.

In this study, image analyses were conducted after all the time-lapsed images were

captured. However, real-time image analyses might be required in order to utilize the algorithm for the detection of the tips of MTs in the nano-scale transport systems. In the case that the algorithm was applied to a single image of kinesin-driven MTs with the size of 512 × 512 pixels and binarization was conducted automatically using pre-set threshold level, we confirmed that the tips of the MTs were extracted within 1 s. Since the gliding velocity of MTs *in vitro* were almost 1 μm/s at fastest[18], the algorithm in this study will be practically useful under systems capturing the images with microscopes.

In summary, we suggested an algorithm for the extraction of the tips of MTs from fluorescent images as markers of the positions of the gliding MTs. The algorithm was initially applied to drawn segments for verification of the algorithm, and results showed that changes in lengths and curvature radii of the segments did not affect errors in the tip extraction, but width of the segments affected the errors by nearly a half of their widths. However, the widths of MTs were approximately 3–5 pixels in the fluorescent images, so the errors of the tip extractions using the algorithm were considered to be negligible. By applying the algorithm to images of gliding MTs, tips of these MTs were successfully extracted. Unlike the centers of gravity, the tips of the MTs were in a good agreement with the trajectories of the gliding MTs. This algorithm may be useful for detecting the position of gliding MTs and assist in the development of controls for nano-scale transporters.

Acknowledgements

The authors thank Prof. Hideo Higuchi for technical support during preparation of the proteins. The authors acknowledge the support of the Tohoku University Global COE Program "Global Nano-Biomedical Engineering Education and Research Network Centre".

References

(1) Sheetz, M.P., Vale, R., Schnapp, B., Schroer, T., and Reese, T., Vesicle movements and microtubule-based motors, *Journal Cell Science*, Vol. 5, (1986), pp. 181–188.

(2) Schroer, T.A., Schnapp, B.J., Reese, T.S., and Sheetz, M.P., The role of kinesin and other soluble factors in organelle movement along microtubules, *Journal of Cell Biology*, Vol. 107, No. 5 (1988), pp.1785–1792.

(3) Diez, S., Reuther, C., Dinu, C., Seidel, S., Mertig, M., Pompe, W., and Howard, J., Stretching and transporting DNA molecules using motor proteins, *Nano Letters*, Vol. 3, No. 9 (2003), pp. 1251–1254.

(4) Ramachandran, S., Ernst, K.H., Bachand, G.D., Vogel, V., and Hess, H., Selective loading of kinesin-powered molecular shuttles with protein cargo and its application to biosensing, *Small*, Vol. 2, No. 3 (2006), pp. 330–334.

(5) Hess, H., Matzke, C.M., Doot, R.K., Clemmens, J., Bachand, G.D., Bunker, B.C., and Vogel, V., Molecular shuttles operating undercover: A new photolithographic approach for the fabrication of structured surfaces supporting directed motility, *Nano Letters*, Vol. 3, No. 12 (2003), pp. 1651–1655.

(6) Howard, J., Hudspeth, A.J., and Vale, R.D., Movement of microtubules by single kinesin molecules, *Nature*, Vol. 342, No. 9 (1989), pp. 154–158.

(7) Suzuki, H., Yamada, A., Oiwa, K., Nakayama, H, and Mashiko, S., Control of actin moving trajectory by patterned poly (methylmethacrylate) tracks, *Biophysical Journal*, Vol. 72, No. 5 (1997), pp. 1997–2001.

(8) Riveline, D., Ott, A., Julicher, F., Winkelmann, D.A., Cardoso, O., Lacapère, J.J., Magnúsdóttir, S., Viovy, J.L., Gorre-Talini, L., Prost, J., Acting on actin: the electric motility assay. *European Biophysical Journal*, Vol. 27, No. 4 (1998), pp. 403–408.

(9) Hiratsuka, Y., T. Tada, K. Oiwa, T. Kanayama, and T.Q. Uyeda. Controlling the direction of kinesin-driven microtubule movements along microlithographic tracks, *Biophysical*

Journal, Vol. 81, No.3 (2001), pp. 1555–1561.

(10) Moorjani, S.G., Jia, L., Jackson, T.N., and Hancock, W.O., Lithographically patterned channels spatially segregate kinesin motor activity and effectively guide microtubule movements, *Nano Letters*, Vol. 3, No. 5 (2003), pp. 633–637.

(11) Hess, H., Matzke, C.M., Doot, R.K., Clemmens, J., Bachand, G.D., Bunker, B.C., and Vogel, V., Molecular shuttles operating undercover: A new photolithographic approach for the fabrication of structured surfaces supporting directed motility, *Nano Letters*, Vol. 3, No. 12 (2003), pp. 1651–1655.

(12) van den Heuvel, M.G., de Graaff, M.P., and Dekker, C., Molecular sorting by electrical steering of microtubules in kinesin-coated channels, *Science*, Vol. 312, No. 5775 (2006), pp. 910–914.

(13) Sugita, S., *Fundamental study of nano-scale transporting system utilizing kinesin-driven microtubules*, PhD thesis, Tohoku University, 2008.

(14) Zhang, T.Y. and Suen, C.Y., A fast parallel algorithm for thinning digital patterns. *Communications of the ACM*, Vol. 27 (1984), pp. 236–239.

(15) Sugita, S., Sakamoto, N., Ohashi, T., Sato, M., Characterization of motility properties of kinesin-driven microtubules towards nano-scale transporter: focusing on length of microtubules and kinesin density, *Journal of Biomechanical Science and Engineering*, Vol. 3, No. 4 (2008), pp. 510–519.

(16) Kamei, T., Kakuta, S., and Higuchi, H., Biased binding of single molecules and continuous movement of multiple molecules of truncated single-headed kinesin, *Biophysical Journal*, Vol. 88, No. 3 (2005), pp. 2068–2077.

(17) Anderson, C. M., Georgiou, G. N., Morrison, I. E., Stevenson, G. V., and Cherry, R. J., Tracking of cell surface receptors by fluorescence digital imaging microscopy using a charge-coupled device camera. Low-density lipoprotein and influenza virus receptor mobility at 4 degrees C, *Journal of Cell Science*, Vol. 101, (1992), pp. 415–425.

(18) Böhm, K.J., Stracke, R., and Unger, E., Speeding up kinesin-driven microtubule gliding *in vitro* by variation of cofactor composition and physicochemical parameters, *Cell Biology International*, Vol. 24, No. 6 (2000), pp. 335-341.

Biorheology 46 (2009) 93–105
DOI 10.3233/BIR-2009-0528
IOS Press

Review

Biomechanical properties of actin stress fibers of non-motile cells *

Shinji Deguchi [a,b] and Masaaki Sato [a,b,**]
[a] *Graduate School of Biomedical Engineering, Tohoku University, Sendai, Japan*
[b] *Graduate School of Engineering, Tohoku University, Sendai, Japan*

Received 21 November 2008
Accepted in revised form 11 February 2009

Abstract. The structure of stress fibers, contractile actin bundles, differs between motile and non-motile cells, though the same term "stress fiber" is used to refer to the structurally as well as functionally different actin bundles. Stress fibers in non-motile cells run between separate focal adhesions, producing isometric tension due to actomyosin contraction. The stress fiber contraction is maintained through dynamic molecular exchanges between preformed and cytoplasmic components. This isometric contraction has been recognized as being essential for extracellular matrix assembly and resultant wound healing. In addition, there have recently been increasing data suggesting that stress fibers under contraction by themselves work as a mechanosensitive element. In this review we discuss, from molecular and physical viewpoints, biomechanical properties of the stress fiber of non-motile cells such as contraction force, resistance to stretching, and their roles in keeping a mechanical homeostasis, which play vital roles in the mechanosensing process.

Keywords: Stress fiber, isometric contraction, mechanical properties, mechanotransduction, actin filament, myosin, α-actinin

1. Introduction

Stress fibers are contractile actin bundles [34]. The bundles are cross-linked by α-actinin, and their contractility is realized by the interaction between actin and double-headed myosin II motor protein with tropomyosin. Such actin bundles containing those proteins appear in both motile cells and non-motile cells [7] and are referred to as a stress fiber in distinction to other actin-based cytoskeletal structures, the lamellipodial actin network or filopodial actin bundles [45]. There have, however, been increasing reports suggesting that structures and functions of stress fibers are different in motile cells and non-motile cells.

Stress fibers in non-motile cells such as vascular endothelial cells elongate and orient in a specific direction in response to fluid shear stress [62] or substrate stretching [31]. The dynamic changes in stress

*This article is based on a plenary lecture given by Dr. Sato at the 13th International Congress of Biorheology and 6th International Conference of Clinical Hemorheology at the Pennsylvania State University, State College, PA, USA, July 9–14, 2008.

**Address for correspondence: Dr. M. Sato, Graduate School of Biomedical Engineering, Tohoku University, Sendai 980-8579, Japan. Tel.: +81 22 795 5017; Fax: +81 22 795 5018; E-mail: sato-m@bme.tohoku.ac.jp.

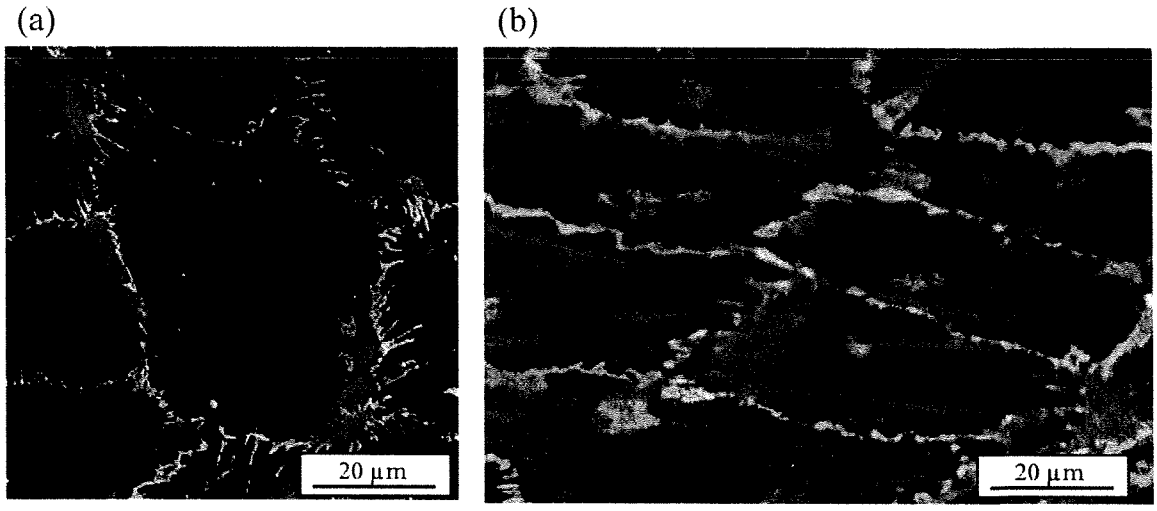

Fig. 1. Typical morphological changes of human umbilical vein endothelial cells in response to fluid shear stress. (a) Static condition: red are actin filaments; green is VE-cadherin. (b) Cells elongate in the flow direction (from the left to right) after exposure to shear. (The colors are visible in the online version of the article.)

fiber (Fig. 1) in concert with focal adhesion remodeling are regulated by a signaling cascade involving the RhoA small GTPase [5,28,50]. Previous studies have demonstrated that, in addition to the activations of Rho and its downstream effectors Rho-kinase and mDia, mechanical stress by itself affects the stress fiber remodeling [20,31]. Stress fibers in non-motile cells are contracted in an ATP-dependent manner while keeping a constant length between fixed focal adhesions (i.e., isometric contraction). Hence, tensions are always present in stress fibers even in the absence of external loading such as fluid shear stress and substrate stretch. The isometric contraction allows extracellular matrix (ECM) assembly and resultant wound healing [16,48,64]. Recent studies have demonstrated that changes in the isometric contraction caused by external loadings, such as alteration in tension or stress level, affect the molecular dynamics responsible for the contraction, and as a result elicit mechanosensitive responses of stress fibers.

Biomechanical properties of stress fibers including contractile behavior and resistance to mechanical loading would therefore have an important influence on their mechanosensing process. In this review, after emphasizing the differences in stress fibers between motile and non-motile cells, we discuss the biomechanical properties and behaviors of the stress fibers of non-motile cells based on reported measurement data and analyses.

2. Structural differences of stress fibers between motile and non-motile cells

To understand the contraction mechanism of stress fibers, knowledge of the actin filament polarity inside of the stress fiber is the most basic because it provides the direction of myosin motor movement along actin filaments (i.e., from pointed or minus end to barbed or plus end). Cramer et al. [7] detected the polarity by electron microscopy using myosin subfragment-1 head decoration. Spatial orientations of individual actin filaments along stress fibers were different between motile and non-motile cells, though the same term "stress fiber" is often used to refer to such structurally and functionally different actin bundles. Characteristics of the structures are schematically shown in Fig. 2 based on Cramer's

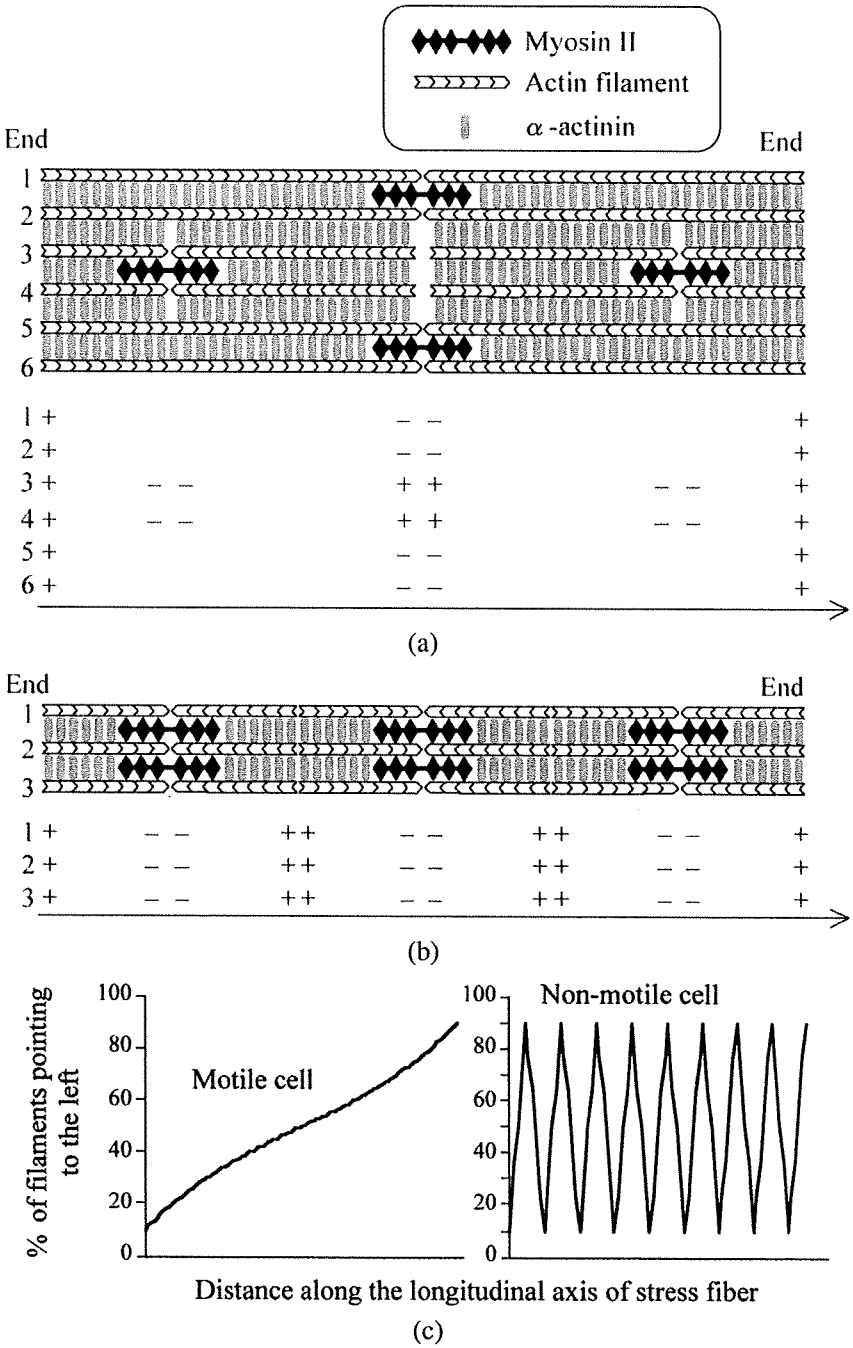

Fig. 2. Schematic drawing of the structural differences between the stress fiber in motile cells and non-motile cells based on Cramer's observations [6]. (a) Ventral stress fiber in motile cells, showing orientations of actin polarity. (b) Ventral stress fibers in non-motile cells. (c) Stress fibers in motile cells have a graded polarity pattern along the long axis (left), whereas those in non-motile cells have a periodic alternation similar to a muscle sarcomere. Modified from Cramer et al. [6] with permission of the copyright holder (The Rockefeller University Press).

observations. In the ventral region of migrating cells having inverted triangular morphology (primary fibroblasts), predominant orientations of individual actin filaments gradually alter along stress fibers. Specifically, barbed ends of actin filaments present at the ends of a stress fiber are directed toward focal adhesions (Fig. 2(a)). Around middle regions of the same stress fiber, the actin filament orientations are mixed, with the result that stress fibers in the ventral region of the motile fibroblasts exhibit a graded polarity pattern (Fig. 2(c)).

In contrast, stress fibers in the ventral region of non-motile cells (PtK2 cells) typically show a periodic alternation of the polarity (Fig. 2(b)). Reflecting this, myosin II and α-actinin appear alternately along stress fibers (Figs 2(c) and 3), similar to the organization of the muscle sarcomere (Fig. 4). The spatial periodicity is 0.9 μm in epithelial cells (PtK2 cells) and 1.5 μm in fibroblasts (Gerbil fibroma) [51]. The muscle sarcomeric configuration suggests that the stress fiber in the ventral region of non-motile cells, which is the subject of this commentary, is highly contractile and plays essential roles in isometric tension generation and resultant ECM assembly [36], whereas the ventral stress fiber in motile cells seems less suitable for generation of such static isometric tensions [48]. This review does not touch on the stress fibers present at other portions of non-motile cells, such as apical stress fibers running between the ventral and apical cell membranes, which become particularly prominent in response to fluid shear stress [26,27,30].

Stress fibers in the cytoplasm are a highly dynamic structure even in stationary cells [31,47,49], implying that such rapid association/dissociation kinetics of molecules may be essential for the formation and contractility of the stress fibers [28]. Live cell microscopy focusing on how stress fibers are assembled and disassembled may provide hints on the polarity of individual actin filaments. Hotulainen and Lappalainen [21] observed dynamics during stress fiber assembly, though it was for motile cells (U2OS cells) similar to fish keratocytes in shape having half-moon morphology [14]. They found that actin polymerization towards the cytoplasm was driven by formin (mDia1/DRF1) at focal complexes (i.e., small focal adhesions), and that connections of multiple actin bundles followed by their own contractions yield a stress fiber running between separate focal complexes in ventral regions. On the other hand, the assembly mechanism of the stress fiber in non-motile cells remains unclear; yet, another actin bundle in motile

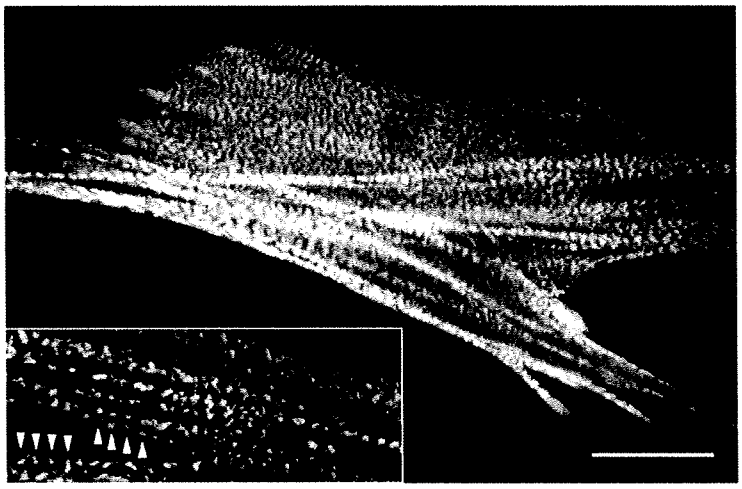

Fig. 3. A smooth muscle cell expressing GFP-α-actinin. Bar: 10 μm. Inset: magnified view; arrowheads denote periodic staining patterns seen along stress fibers.

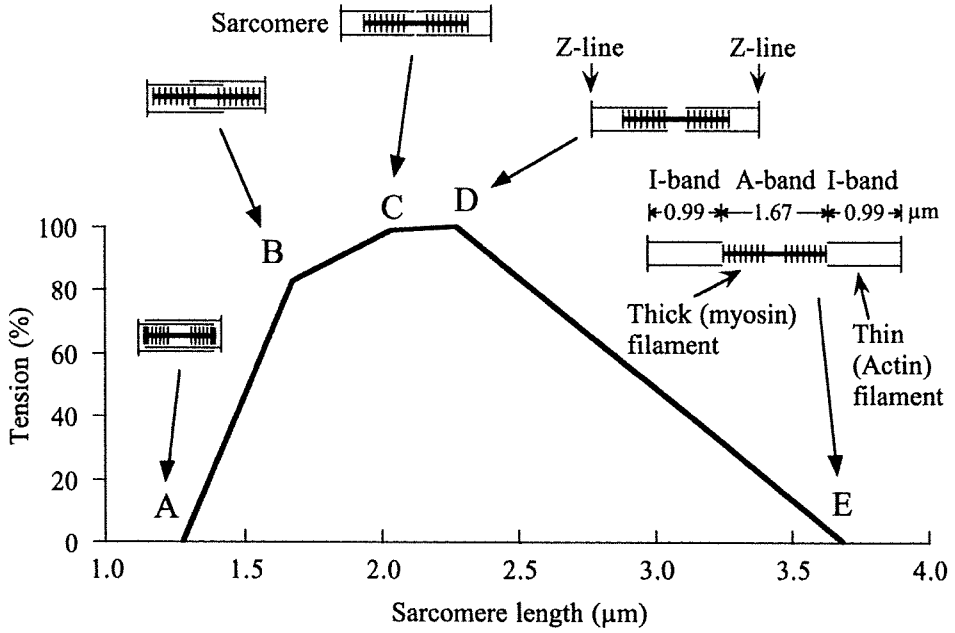

Fig. 4. Active tension generated by muscle sarcomere as a function of its length. Modified from Fung [11] with permission of the copyright holder (Springer).

cells, generated in the proximity of the cell membrane and referred to as transverse arc, has an alternate α-actinin–myosin II structure [7,21]. This transverse arc finally becomes the ventral stress fiber in motile cells having focal adhesions at both ends, thus similar in structure to the stress fiber in non-motile cells. Judging from the similar structures, the unknown assembly mechanism of the stress fiber in non-motile cells may be comparable to that of the ventral stress fiber in motile U2OS cells. In addition, Hirata et al. [20] observed the dynamics of actin bundle formation from individual actin filaments using semi-intact fibroblast cells, demonstrating that stress fibers are aligned parallel to the direction of externally applied tension.

3. Isometric tension and its relationship to assembly/disassembly

Hereafter, stress fibers in non-motile cells are the topics of discussion. Stress fibers are anchored to ECM at both ends via focal adhesions. Actomyosin contraction then produces isometric tension even in the absence of extracellular forces. Activation of myosin regulatory light chain (MLC) by Rho-kinase is responsible for the contraction, which modulates organization of stress fibers and focal adhesions [3]. Rho-kinase phosphorylates MLC directly as well as through inhibition of myosin phosphatase [24]. Meanwhile, it has been reported that calmodulin and MLC kinase (MLCK) specifically activate stress fibers lying at the cell periphery in fibroblasts in a Ca^{2+}-dependent manner [28]. They demonstrated that more rapid and extensive stress fiber contraction is induced by MLCK than by Rho-kinase. This selectivity probably holds true for endothelial cells as well because inhibition of Rho-kinase activity by Y27632 attenuated stress fiber formation particularly in central regions of the cells [31]. Different from the traction force generated by stress fibers in motile cells that is less suited for static contraction

[13,48], the isometric contraction plays critical roles in ECM assembly and resultant wound healing [16,19,64]. The MLCK-regulating contraction of peripheral stress fibers might be used for the maintenance of intercellular junctions, rather than wound healing, because those thick peripheral stress fibers or dense peripheral bands become prominent in confluent cells. Katoh et al. [28] suggested that the Ca^{2+}-regulating MLCK system is used to generate rapid contraction because Ca^{2+} release in cells is rapid and transient in general. Meanwhile, they considered that the Ca^{2+}-independent Rho-kinase system plays a major role in maintaining sustained contraction (and hence isometric contraction) in cells because, once MLC is phosphorylated, the activated state allowing contraction can be maintained by inhibiting the myosin phosphatase.

Immediate disassembly of stress fibers occurs when the tension is released by compressing. Costa et al. [6] revealed the existence of a threshold strain value required for inducing the tension-dependent disassembly. They observed, just before the occurrence of the disassembly, buckling of stress fibers in non-motile endothelial cells after compressive loading. Reasoning that the buckling occurred at their unloaded slack length, stress fibers were estimated to have a 15–26% prestrain. The variability of the value was possibly dependent on where the stress fibers were located in cells. Sato et al. [52] quantified by strain analysis on each fiber in osteoblastic cells that a compressive strain of ~20% induced disassembly. Furthermore, Lu et al. [39] found that the prestrain of stress fibers in endothelial cells increased from 10% to 26% when treated with 2 nM calyculin A that is a serine/threonine phosphatase inhibitor elevating MLC phosphorylation, and on the other hand decreased to 5% when treated with 10 μM blebbistatin that is a selective inhibitor of actomyosin interactions with a high affinity for myosin II [49]. These results indicate that stress fibers under isometric contraction have a definite tensional strain dependent on the degree of actomyosin interaction. It is, however, important to note that the matter may not be so simple since stress fibers after severed at the middle regions by laser cutting retracted due to existing tension but were not disassembled, although the tension release was transmitted to the end focal adhesions via the stress fibers [35].

Goffin et al. [16] indicated that not only strain but also tensional stress is kept an intrinsic value in myofibroblasts. They found that an ~12 nN/μm^2-tensional stress (i.e., force per unit focal adhesion area) exists at "supermature" focal adhesions [19] having large focal adhesion sizes (>7.5 μm^2), whereas a stress of only 3.8 nN/μm^2 exists at small focal adhesions or focal complexes (≤7.5 μm^2). With the changes in area size, stress fibers connecting serially the focal adhesions thus seem to keep the tensional stress as well as strain constant. The higher stress in large focal adhesions compared to small focal complexes was realized firstly by remodeling of ECM to create larger surfaces for adhesion that permit efficient tension transmission and development of stress fibers. Subsequently, the high contractility was enhanced by recruitment of α-smooth muscle actin, suitable for generating high contractility [18], to the stress fibers preformed from β-actin. The change in actin isoforms depending on mechanical conditions seems similar to the isoform changes from β-actin or γ-actin to α-actin seen during skeletal or cardiac muscle sarcomere assembly [11,38].

The phenomenon that constant prestrain and prestress are maintained, therefore, indicates that cells keep a mechanical homeostasis [23,44] associated with strain and stress in stress fibers. The jump of the maintained prestress, reported by Goffin et al. [16], from small focal complexes (3.8 nN/μm^2) to supermature focal adhesions (12 nN/μm^2) could be interpreted, from the standpoint of physics, as a transition from one equilibrium state to another: in each equilibrium state, a certain definite strain or stress should be kept. Cells may thus adapt to a slight change in the environment while keeping the mechanical homeostasis only using existing proteins. Actually, it is known that the size of mature focal adhesions reversibly increases and decreases as a function of applied force [15]. Meanwhile, if the change in the